LAWRENCE
LIVERMORE
NATIONAL
LABORATORY

LLNL-JRNL-656683

Eliminating Underconstraint in Double Parallelogram Flexure Mechanisms

R. M. Panas, J. B. Hopkins

July 7, 2014

Journal of Mechanical Design

Disclaimer

Eliminating Underconstraint in Double Parallelogram Flexure Mechanisms

Robert M. Panas[1], Jonathan B. Hopkins[2], Veronica Szklarzewski[3], Elizabeth C. Schanne[3]

[1]Lawrence Livermore National Laboratory, L-229

7000 East Avenue, Livermore, CA 94551

[2]University of California, Los Angeles

Mechanical and Aerospace Engineering

Los Angeles, CA 90095

[3]Massachusetts Institute of Technology

Department of Mechanical Engineering

Cambridge, MA 02139

We present an improved flexure linkage design for removing underconstraint in a double parallelogram linear flexural mechanism. This new linkage alleviates many of the problems associated with current linkage design solutions such as static and dynamic performance losses and increased footprint. The improvements of the new linkage design will enable wider adoption of underconstraint eliminating (UE) linkages, especially in the design of linear flexural bearings. Comparisons are provided between the new linkage design and existing UE designs over a range of features including footprint, dynamics and kinematics. A nested linkage design is shown through Finite Element Analysis (FEA) and experimental measurement to work as predicted in selectively eliminating the underconstrained Degree-of-Freedom (DOF) in double parallelogram linear flexure bearings. The improved bearing shows an 11x gain in the resonance frequency and 134x gain in static stiffness of the underconstrained DOF, as designed. Analytical expressions are presented for designers to calculate the linear performance of the nested underconstraint eliminator linkage (average error <5%). The concept presented in this paper is applied to an analogous double-nested rotary flexure design.

Keywords: dynamics; underconstraint elimination; four-bar flexure; folded flexure; double parallelogram flexure; double tilted beam flexure; exact constraint folded flexure; nested linkage; flexure mechanism

1. Introduction

The intent of this work is to improve the linkage mechanism that selectively removes the underconstraint in double parallelogram (DP) linear flexure bearings, without sacrificing the benefits of the flexural bearing. Existing linkage design solutions [1–3] present significant tradeoffs with a range of disadvantages including asymmetry, static and dynamic performance losses, increased bearing footprint, parasitic kinematic error, and design coupling, all of which limit the applicability of the underconstraint eliminator (UE) designs. An improved nested linkage mechanism is presented as shown in Fig. 1 which is able to provide similar UE performance without many of these limitations. This results in increases in range, dynamic stability, and bandwidth, in conjunction with reductions in footprint and parasitic kinematic error. The improved linkage design can be used in a wider range of machine designs than existing UEs, and can be used to replace existing UE linkages, resulting in performance increases. Detailed models are provided for the small displacement behaviors as well as dynamics.

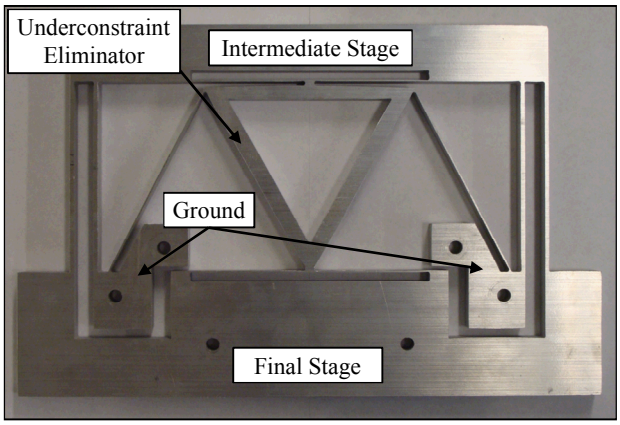

Fig. 1. Flexure DP with nested UE linkage. This linkage selectively removes the underconstraint inherent in the DP design by linking the motion of the intermediate and final stage.

Flexure bearings are often used in precision machine design [4–6] for many reasons, including i) fine resolution as friction is zero and hysteresis is minimal, ii) no backlash, iii) no power draw due to the passive nature of the components, iv) the possibility of achieving complex kinematics [7,8], v) ease of integration of

low-cost high performance sensing [9], vi) largely linear elastomechanics, and vii) ease of fabrication at low-cost due to their often monolithic structure. Flexures also have significant disadvantages, one of which is their limited range of motion [6].

Stacked stage designs, utilizing flexure bearings in series, are a common solution to the range limitation [4,6]. One such design, also called a double parallelogram flexure bearing, is shown in Fig. 2a, which is two four-bar flexure parallelograms in series to double the range of the linear bearing. This linear bearing geometry will be the focus of the paper.

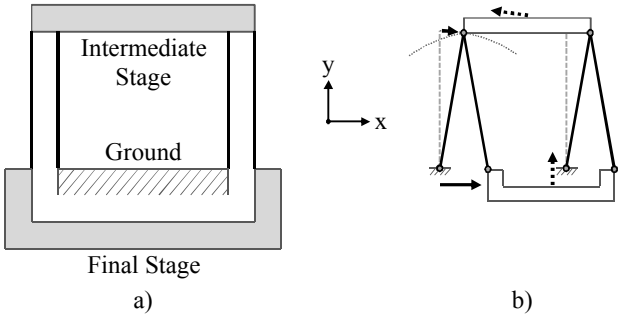

Fig. 2. a) DP linear bearing with components labeled. Possible motions for the structure are shown in an equivalent linkage model in b). The solid arrows show the nominal translational motion, with the kinematic errors canceled by geometry reversal. The dotted arrows show the y-axis DOF for the structure observed at large displacements, which is revealed as a drop in axial stiffness.

DP flexures are used in many instances, including single or multi-axis precision positioning stages [10–15], linear bearing elements in macroscale machines [6,16–19], or in MEMS devices [3,11,20–28]. These elements have received significant attention and analysis in literature, several noteworthy examples of which are suggested here for the reader's further study [1,6,10,17,19,29–31].

DP flexure bearings have several advantages and disadvantages which must be considered during design. The advantages of the serial stages include increased range and reduced parasitic kinematic errors. The arcuate parasitic kinematics errors of each of the flexure bearings can be cancelled out via geometry reversal to generate nearly ideal linear motion. This cancellation requires that the intermediate stage traverse approximately half the final stage displacement, in phase with the final stage [1,6,10,17,19,29]. The cancellation effect is shown in the effective linkage model shown in Fig. 2b with the solid arrows.

There are several disadvantages to serial parallelogram stages, including dynamic and axial stiffness issues. This is because the intermediate stage possesses the same translational DOF as the final stage [6].

The redundant DOF causes the intermediate stage to be underconstrained because it is free to move even when the final stage is held fixed relative to the ground [5,6,10,19,32].

The underconstraint appears as an extra, uncontrolled DOF of the bearing [6,19]. The underconstrained intermediate stage DOF has a relatively low resonance frequency which is generally on the same scale as the main translational DOF resonance of the main stage, due to the similar scale of both DOF stiffnesses and (typically) the masses. This underconstrained resonance is associated with collocated dynamics, where the sensor and actuator are on a single rigid body, while a separate body in the system is able to resonate [33]. This generates stability issues, leading to difficulty in precise control, especially when the collocated dynamics are close to the cross-over frequency, as is typically found with the underconstrained intermediate stage [14,15].

The underconstraint enables a y-direction DOF for the final stage at large displacements as shown in Fig. 2b via the dotted arrows. The intermediate stage slides back along its arcuate trajectory towards equilibrium, allowing the final stage to translate in the y-direction [1,10,31]. The motion of the intermediate and final stages are no longer linked by a 2:1 ratio in this vertical DOF, as they are for the main translational DOF. The y-direction corresponds to axial loading on the flexures, which is a high-stiffness degree-of-constraint at low displacements. The axial stiffness thus drops dramatically at large displacements [1,2,10,23,30], due to the allowed motion shown by the dotted arrows.

2. Background

A review is presented of previous design solutions for the removal of underconstraint in flexure DP bearings. R.V. Jones suggested a multi-body lever linkage solution to this issue in 1956 [29], based on a suggestion by Plainevaux [34,35] of coupling the intermediate and final stage via a gearing system. Smith [36] describes a modification of Jones' design in which the sliding contacts are replaced with flexure joints, but retains an apparently assembled pin joint for linking the lever arm to ground. All of these designs remove underconstraint, however they introduce several drawbacks which can negate some of the benefits of flexural bearings. These designs utilize non-flexural bearings which introduce several acknowledged problems [29] including requiring assembly, generating an asymmetric effect, and introducing friction. The problems were solved via later UE designs, as described below, which utilize only flexural joints and thus regain the benefits

of the flexural bearing in terms of friction and fine motion control. This paper considers a usable UE design as one which will not negate the benefit of flexural bearings. The Jones, Plainevaux and Smith designs will thus not be included in further comparison.

Many designs that do not meet the criteria of being usable UEs have been suggested to improve the performance of the DP linear bearing, and several (but by no means all) are noted here for illustrative purposes. These include combining the DP with angled flexure bearings [24,26], pre-bending the flexures [20,26], linking the intermediate stages of symmetric bearing sets [25], angling 4-bar beams out-of plane [37], or introducing a lever arm held in place entirely with parallel blades [38]. While these designs address some of the symptoms of underconstraint, they either do not remove all of the underconstrained DOFs [20,24–26], or they introduce new DOFs to the final stage [37,38]. Thus these designs retain at least one more DOF beyond the single desired translational DOF, which is the underlying problem we seek to resolve. This paper focuses on comparing designs which fully remove the underconstraint in the flexural linear bearing, so the abovementioned papers will not be included in further comparison.

2.1. Double tilted-beam flexure bearing

The double tilted-beam flexure bearing design, shown in Fig. 3a, has been suggested as one means of removing underconstraint via angling the flexure beams, [1,3,24,26]. This design adjusts each of the beams off from vertical (y-direction) by an equal angle to create two instant centers, one below and one above the bearing. The intermediate stage of this design is no longer underconstrained because each flexure bearing module possesses non-redundant instant center rotational DOFs. In the case where multiple bearing elements are desired/allowed, this bearing provides the additional benefit that the underconstraint elimination in this mechanism is all done with the four existing flexures. The multiple bearing requirement is due to the need to negate the second DOF intrinsic to the bearing design, as shown in Fig. 3 and explained below.

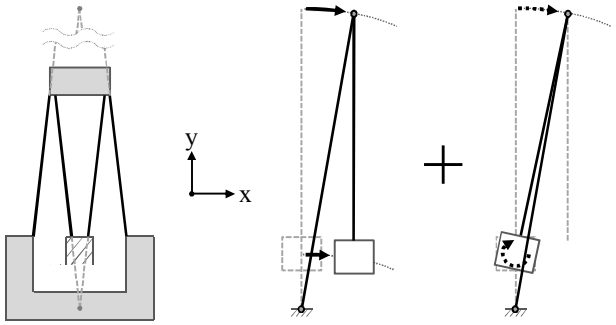

Fig. 3. a) Double tilted-beam linear bearing shown on left with instant centers identified. The two possible motions for the structure are shown in equivalent linkage models in b). The solid arrows show the nominal translational motion where the final stage does not rotate. Note that the kinematic errors are not canceled in this translation. The dotted arrows show the extra DOF of the structure where the final stage rotates without translating.

Such a design poses several disadvantages however, including design coupling, altered DOF and parasitic kinematics. The performance of the main translational DOF is now coupled with the performance of the UE from an axiomatic design perspective [39] via angling of the beams. The coupling of multiple functional requirements to the same design parameters (tilt angle) results in a reduced design space. The main translational elastomechanics are altered by angling the beams, resulting in increased stiffness [1] due to the combined translation and rotation in the beams. The outer set of flexures in Fig. 3a will be further loaded by the intermediate stage rotation, increasing stress buildup [3], and thus reducing total bearing range. The final stage shows an extra DOF in the tilted-beam design as shown in the equivalent linkage model in Fig. 3b. The final stage can either move along an arcuate path as shown by the solid arrows or rotate as shown by the dotted arrows. This design returns to being a 1DOF translational bearing only if the rotation is constrained [1]. To do so requires multiple structures, such as using two of these bearings side-by-side or end-to-end. Full bearing performance thus requires at least approximately twice the footprint of a single bearing. Finally, the parasitic kinematic errors are not canceled [1] in this design. The two bars in series do not carry out equivalent motions, shown in Fig. 3b by the solid arrows. The first bar rotates, while the second translates. Thus the final stage follows an arcuate path whose radius is the separation between the two instant centers, and the stage motion is left with a cosine-like y-direction parasitic error motion at large displacement [1].

2.2. Exact constraint folded flexure with external linkage

The exact constraint folded flexure bearing design, shown in Fig. 4a, has also been suggested as a means of removing underconstraint, [2,11,19,31,37,40,41]. This design is based on the assembled lever arm suggested by Jones [29], and utilizes an external linkage to tie the kinematics of the intermediate stage to the final stage. The rigid linkage rotates around an instant center above the bearing, shown in the equivalent linkage model in Fig 4b. The distance from this instant center to each of the stages sets the allowed ratio of motion between the stages. This ratio is fixed at a 2:1 ratio to ensure that the intermediate stage translates half as far as the final stage, as shown by the solid arrows in Fig. 4b, thus removing the underconstrained DOF but not interfering with the kinematics of the main translational DOF.

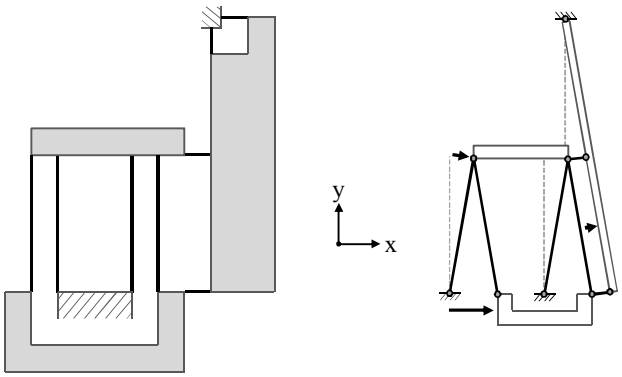

Fig. 4. a) Exact constraint folded flexure utilizing an external linkage. The possible motion for the structure is shown in the equivalent linkage model in b). The solid arrows show the nominal translational motion, which is equivalent to the DP flexure bearing alone.

The external linkage design possesses several drawbacks including degraded dynamics, asymmetry, and increased footprint. The external linkage can significantly alter the dynamics of the main translational DOF via the asymmetric layout and the added inertia [6,17]. The higher dynamics are also impacted by this extra mass. The asymmetric layout of the bearing increases its thermal sensitivity [6,17]. Finally, the inclusion of the large linkage roughly doubles the required bearing footprint.

3. Nested Linkage Designs

3.1. Linear Bearing Design

The new design presented here draws upon the design of the external linkage exact constraint folded flexure described above. The modification is intended to fix the main drawbacks of the external linkage design- dynamics, symmetry and footprint. The instant center of the added linkage is placed along the plane of symmetry of the structure, as shown in Fig. 5a, which passes through the middle of the device. This placement improves the dynamics and symmetry of the structure. The linkage guiding flexures (labeled 2 in Fig. 5a) do not need to extend all the way to the instant center- instead both these flexures and the linkage itself can be designed to nest within the central dead-space in the double-parallelogram. This reduces footprint and inertia for the linkage. The linkage is shaped in a triangular fashion with hollowed center to maximize the stiffness of the body with the least additional mass. It is attached to each of the stages with sets of blade flexures (labeled 1 in Fig. 5a) axially aligned to the final and intermediate stage DOF along the x-axis. These blade flexures are included symmetrically to avoid buckling, thermal sensitivity and dynamic issues. The type 1 blade flexures may be replaced with wire flexures to avoid overconstraining the structure.

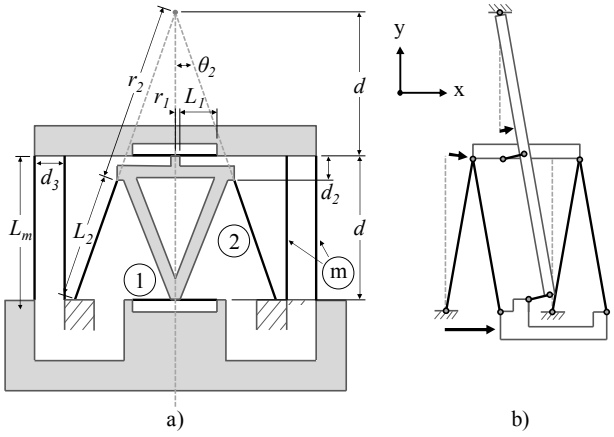

Fig. 5. a) Exact constraint folded flexure design with an improved, nested linkage for UE. The possible motion for the structure is shown in the equivalent linkage model in b). The solid arrows show the nominal translational motion, which is equivalent to the DP flexure bearing alone.

The nested linkage must be able to access both stages and the ground in order to kinematically link the stages. The point of contact of the linkage to each of the stages may be at any height, it does not need to be at the surface defined by the end of the four main flexures (labeled m in Fig. 5a). By moving these points of contact closer to one another, the location of the instant center for the linkage is shifted. The location of the

instant center sets the angle at which the type 2 flexures (labeled 2 in Fig. 5a) contact the linkage, and thus how stiff they are when resisting the translational DOF of the intermediate stage. The type 2 flexures will need to displace roughly as much as the main flexures. These type 2 flexures are typically thinner than the type m flexures in order to avoid significantly altering the main translational DOF, so they see lower stresses than the main type m flexures. This means that the addition of the UE will not typically change the range of the overall flexure bearing.

3.2. Rotary Analog Design

The UE linkage concept is extensible to different flexure mechanisms that achieve other kinds of motions. A double nested rotational flexure analog to the translational version presented previously is shown in Fig. 6a. This compact flexure topology can enable large rotational motion in a similar way to how the double parallelogram flexure bearing in Fig. 2 achieves pure translational motion. If the intermediate stage shown in Fig. 6a were grounded, the final stage could still rotate about the axis shown as a red dot with a circular arrow, but this axis of rotation would immediately begin to drift left or right depending on the direction the stage were rotated for finite deformations. To eliminate this unwanted parasitic error effect while dramatically increasing the mechanism's rotational range without increasing its overall footprint, the intermediate stage shown in Fig. 6a should be free to rotate half the number of radians as the final stage while the labeled ground is held fixed as shown. The necessary lengths and orientations of the four flexure blades to maintain the location of the intended rotational axis over finite rotations (for when the intermediate stage rotates half the radians as the final stage) can be determined using the mathematics provided by Van Eijk [19]. The system retains an underconstrained DOF even after the flexure lengths are correctly chosen. The underconstraint causes many of the same dynamic problems discussed previously for the translational analog mechanism in Fig. 2. This can be solved by inserting an analogous symmetric UE linkage similar to the one shown in Fig. 5. Whereas the UE linkage in Fig. 5 rotates to ensure that its mechanism's intermediate stage translates half as much as its final stage, the UE linkage analog in Fig. 6b translates to ensure that its mechanism's intermediate stage rotates half as much as the final stage. Note that as long as the two distances labeled h in Fig. 6b are equal, the mechanism's intermediate stage will rotate $\sim d/2h$ radians as its final stage rotates $\sim d/h$ radians where d is the distance the UE linkage translates (Fig. 6c). The vertical flexure bearings only permit this linkage to translate horizontally as shown by the arrow in Fig. 6c.

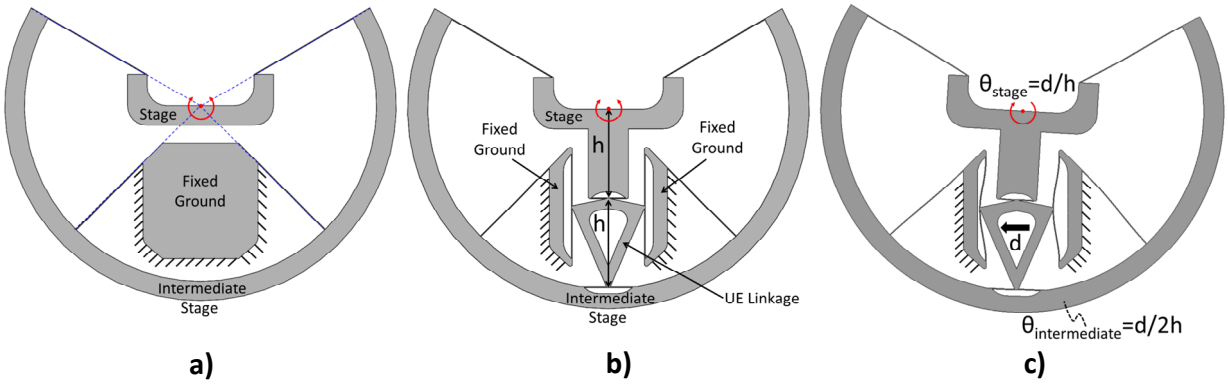

Fig. 6. Double nested rotary flexure a), similar flexure but with a UE linkage inserted b), the final stage is forced to rotate twice as many radians as the intermediate stage in the same direction c).

4. Comparison

The three linear bearing designs described above, i) tilted-beam, ii) external linkage, and iii) nested linkage, all eliminate the underconstraint in the DP flexure bearing. Such UE designs increase the displaced axial stiffness (y-direction) of the final stage [1,2] and raise the resonance frequency associated with the underconstrained DOF. The secondary effects of these designs differ, however, as shown in Table 1. Table 1 is included as a designer reference to summarize the general strengths and weaknesses of the three UE designs that have been discussed in detail in the previous sections. This comparison is explicitly carried out independently of a particular design or situation and as such is intended as a qualitative guide for concept level design selection.

Table 1. Comparison of UE designs

	Tilted-Beam	External Linkage	Nested Linkage
Symmetry	+	-	+
Dynamics	+	-	+
Range	-	+	+
Footprint	-	-	+
Kinematics	-	+	+
Design Decoupling	-	+	+

The three designs are standardized in this comparison such that they all equally provide a single linear DOF at the final stage, and utilize identical main bearing flexure geometry. This is to ensure equality in the comparison. The double tilted-beam design must be used in duplicate to do so, resulting in a larger footprint as described previously. Symmetry is maintained and inertia is low for this design due to its simplicity.

These aid the dynamics via minimizing unwanted modes as well as keeping the bandwidth as high as possible. The range is reduced and the design is coupled due to the beam angle as described above. Finally, the main translational DOF will have parasitic kinematics as shown in Fig. 3b. The external linkage design breaks the bearing symmetry, and raises the footprint. The increased mass combined with the asymmetric layout impact the dynamics. The range, kinematics, and design of the main DOF are effectively unaltered by the external linkage design. The improved nested linkage design maintains symmetry, low inertia and footprint via a small hollow linkage nested within the DP. The range, kinematics, and design of the main DOF are also effectively unaltered by the nested linkage design. The nested linkage design has improved performance over the other two common UE designs.

5. Small Displacement Analysis

The equations required to calculate the linear, small displacement static and dynamic performance of the underconstrained DOF are described below. A linear domain analysis of static and dynamic performance is utilized below to provide insight into the capability of the new UE nested linkage design to remove underconstraint. The derivation and implications of the large displacement analysis lies outside the scope of this paper and so will be published separately.

5.1. Final Stage Motion

The linear stiffness, k_f, of the final stage along the main x-axis translational DOF is derived through energy analysis. The energy stored via x-axis translation motion, E_{kf}, is calculated by summing the contributions of each of the flexures as shown in Eq. (1), where r_1 and r_2 are the lever arm for the type 1 and 2 flexures, respectively, d is the separation between the linkage points to the stages, x_f is the x-direction motion of the final stage, and θ_{ue} is the rotation of the UE linkage around its instant center. The geometric variables are indicated in Fig. 5. E, I and L are the Young's modulus, second moment of area, and length respectively of the main (m) flexures, type 1 flexures (1), and type 2 flexures (2). The terms $k_{j\theta}$ describe the j-type flexures' (1 is type 1, 2 is type 2) clamped-free moment-to-rotation stiffness at the free end. The terms k_{jt} describe the j-type flexures' clamped-guided transverse force-to-displacement stiffness at the guided end. The terms $k_{jt\tau}$ describe the j-type flexures' clamped-free moment-to-displacement stiffness at the free end. The bodies are assumed to be rigid for this analysis, motions are assumed to occur in a 2:1 (final to intermediate

stage) ratio, all displacements are assumed to be small, all energy storage along DOC is considered to be negligible, and Euler stiffnesses are used for the beams.

$$E_{kf} = 4\left[\frac{1}{2}k_{mt}\left(\frac{x_f}{2}\right)^2\right] + 4\left[\frac{1}{2}k_{1\theta}\theta_{ue}^2 + \frac{1}{2}k_{1t}\left(r_1\theta_{ue} + \theta_{ue}\frac{k_{1\theta}}{k_{1t\tau}}\right)^2\right]\ldots$$
$$+2\left[\frac{1}{2}k_{2\theta}\theta_{ue}^2 + \frac{1}{2}k_{2t}\left(r_2\theta_{ue} + \theta_{ue}\frac{k_{2\theta}}{k_{2t\tau}}\right)^2\right] \quad (1)$$
$$\theta_{ue} = \frac{x_f}{2d} \quad k_{mt} = \frac{12E_mI_m}{L_m^3} \quad k_{j\theta} = \frac{E_jI_j}{L_j} \quad k_{jt} = \frac{12E_jI_j}{L_j^3} \quad k_{jt\tau} = \frac{2E_jI_j}{L_j^2}$$

The stiffness is calculated by finding the derivative of the energy with respect to x-axis motion on the final stage, as shown in Eq. (2).

$$k_f = \frac{\partial E_{kf}}{\partial x_f}\frac{1}{x_f} = k_{mt} + \overbrace{\frac{k_{1\theta} + \left(k_{1\theta}/k_{1t\tau} + r_1\right)^2 k_{1t}}{d^2} + \frac{k_{2\theta} + \left(k_{2\theta}/k_{2t\tau} + r_2\right)^2 k_{2t}}{2d^2}}^{k_{fue}} \quad (2)$$

The first term on the right hand side contains the contribution from the main flexural DP, labelled type m. The second term describes the combined rotation/translation of the four type 1 flexures, while the third term describes the combined rotation/translation of the two type 2 flexures. The term k_{fue} captures the effect of the UE on the final stage DOF stiffness.

The resonance of the final stage, ω_{nf}, is shown in Eq. (3), where m_f is the mass of the final stage m_i is the mass of the intermediate stage, and m_{ue} is the mass of the UE linkage. The intermediate stage mass is scaled down via a 1:2 transmission ratio. The UE linkage is modeled as a point mass halfway between the intermediate and final stage with a 3:4 transmission ratio.

$$\omega_{nf} = \sqrt{\frac{k_f}{m_f + \frac{1}{4}m_i + \frac{9}{16}m_{ue}}} \quad (3)$$

5.2. Intermediate Stage Motion

The stiffness, k_i, for the intermediate stage x-axis motion (a DOF prior to inclusion of the UE linkage) requires a more complex derivation than that done for the final stage. The inclusion of the UE linkage shifts the intermediate stage motion to occur along a DOC, where rigid body displacement does not follow the simple 2:1 ratio. The flexures are deliberately 'jammed' in this scenario, producing much higher forces, so a free-body-diagram based analysis is more effective than the energy method.

The analysis for the intermediate stage x-axis stiffness is carried out in two steps. First, structural motions are related to the intermediate stage x-axis displacement, x_i. Two main motions are considered: the UE linkage rotation, θ_{ue}, around the instant center formed by the type 2 flexures, and the UE linkage translation, x_{ue}, along the x-axis. Second, the intermediate stage stiffness is derived from these structural motions. The bodies are assumed to be rigid for this analysis, all displacements are assumed to be small, the effects of transverse/moment stiffnesses are considered to be negligible, and Euler stiffnesses are used for the beams. The assumption of axial stiffness dominance over transverse/moment stiffnesses was later confirmed with a full analysis that showed this assumption generated <0.01% error.

The moment and force balance for the UE linkage were derived as shown in Eq. (4), where d_2 is the y-axis separation between the end of the type 2 flexures and the ends of the top type 1 flexures, and θ_2 is the angle of the type 2 flexures off of vertical. The moment balance was carried out around the instant center formed by the type 2 flexures.

$$\begin{aligned}
&\sum F_x = -2k_{11a}\left(x_{ue} - x_i + d\theta_{ue}\right) - 2k_{12a}\left(x_{ue} + d\theta_{ue}\right) - 2k_{2a}\sin(\theta_2)^2 x_{ue} = 0 \\
&\sum M_z = -2dk_{11a}\left(x_{ue} - x_i + d\theta_{ue}\right) - 4dk_{12a}\left(x_{ue} + d\theta_{ue}\right) = 0 \\
&k_{pa} = \frac{A_p E_p}{L_p} \square k_{pb} \qquad \theta_2 = \cos^{-1}\left(\frac{d + d_2}{r_2}\right)
\end{aligned} \tag{4}$$

The subscripts are used to indicate the type 2 flexures (*2*) as well as to separate the type 1 flexures into two sets: the top set (*11*) located at distance *d* from the instant center, and the bottom set (*12*) located at distance 2*d* from the instant center, as shown in Fig. 5. The two sets encounter different deformations in the assumed rigid body of the UE linkage, as will be explained in the rigid body correction section. The terms k_{pa} describe the p-type flexures (*11* is type 1 top set, *12* is type 1 bottom set, *2* is type 2 set) axial force-to-

displacement stiffness. These terms are composed of the flexure axial stiffness in parallel with a rigid body relaxation stiffness, k_{pb}, unique for each flexure set, to account for the failure of the rigid body assumption.

The force and moment balance equations in Eq. (5) are used to calculate θ_{ue} and x_{ue}, as functions of x_i. The UE coordinates are linear functions of the intermediate stage motion, so non-dimensional ratios α_x and α_θ are used as shown in Eq. (5).

$$\begin{aligned}\alpha_x &= \frac{x_{ue}}{x_i} = \frac{2}{1+\sin(\theta_2)^2\left(4k_{11a}^{-1}+k_{12a}^{-1}\right)k_{2a}} \\ \alpha_\theta &= \frac{\theta_{ue}}{x_i} = \frac{\sin(\theta_2)^2 k_{12a}^{-1}k_{2a}-1}{\left[1+\sin(\theta_2)^2\left(4k_{11a}^{-1}+k_{12a}^{-1}\right)k_{2a}\right]d}\end{aligned} \tag{5}$$

The overall structural stiffness of the intermediate stage in the x-axis can now be determined through the known displacement relationships. This is done via an x-axis force summation on the intermediate stage, which combines the main flexures with the type 11 flexures, where F_{ix} is the load applied on the intermediate stage along the x-axis as shown in Eq. (6).

$$\begin{aligned}\sum F_x &= F_{ix} - 4k_m x_i - 2k_{11a}\left(x_i - x_{ue} - d\theta_{ue}\right) = 0 \\ k_i &= \frac{F_{ix}}{x_i} = 4k_{mt} + \overbrace{2\left[\frac{1}{4\sin(\theta_2)^2 k_{2a}} + \frac{1}{k_{11a}} + \frac{1}{4k_{12a}}\right]^{-1}}^{k_{iue}}\end{aligned} \tag{6}$$

The intermediate stage stiffness is extracted from the force summation and Eq. (5), as shown in Eq. (6). This term can be visualized as the main flexures in parallel with the only-UE stiffness, k_{iue}, which is itself composed of two stiffnesses in parallel, each associated with a separate UE motion. The first UE motion is as follows: if $k_{11a} \approx k_{12a} \equiv k_{1a}$ and $k_{1a}/k_{2a} >> 1$ then the type 1 flexures are essentially infinitely stiff along their axis and the UE linkage is thus only able to rotate around the center of stiffness of the type 12 flexure set. The type 2 flexures are scaled via a $[2\sin(\theta_2)]^2$ transmission due to their angle of θ_2 off of vertical. The described motion is captured in Eq. (6) via the k_{2a} term. The second UE motion is as follows: if $k_{2a}/k_{1a} >> 1$ then the type 2 flexures are essentially infinitely stiff along their axis and the UE linkage is thus only able to rotate around the instant center formed by the type 2 flexure set. The type 11 and 12 flexure sets are in series, with the UE

linkage acting as a lever with a 2^2 transmission for the 12 flexures. The described motion is captured in Eq. (6) via the k_{11a} and k_{12a} terms.

The resonance of the intermediate stage, ω_{ni}, is shown in Eq. (7). This expression assumes that the final stage mass is locked in place for simplicity. The UE linkage is again modeled as a point mass halfway between the intermediate and final stage whose displacement normalized to x_i is (α_x+3/2$d\alpha_\theta$). This transmission shifts from 1:2 if k_{2a}/k_{1a}<<1, to 3:10 if k_{2a}/k_{1a}>>1, but in general it lies midway between these values.

$$\omega_{ni} = \sqrt{\frac{k_i}{m_i + \left(\alpha_x + \frac{3}{2} d\alpha_\theta\right)^2 m_{ue}}} \tag{7}$$

5.3. Rigid Body Correction

The rigid body assumption proved to be incorrect when the intermediate stage motion stiffness was analyzed due to the hollow linkage shape and high DOC loading. This section provides the modifications to the expression necessary to account for the rigid body deformation. All of this is contained in the k_{pb} terms, shown in Eq. (4). The rigid body assumption of $k_{pb}\rightarrow\infty$ was initially used, resulting in a predicted k_i=6.70MN/m which closely matches FEA results (6.68MN/m) when the rigid bodies are set to have a Young's modulus that is 10^{10} times the flexure modulus. This value is significantly above the measured and FEA values (≈5MN/m) as shown in Table 2. The deformation of the bodies can clearly not be ignored as while the equations accurately predict ideal rigid body motion, they are off by 25% for the real system.

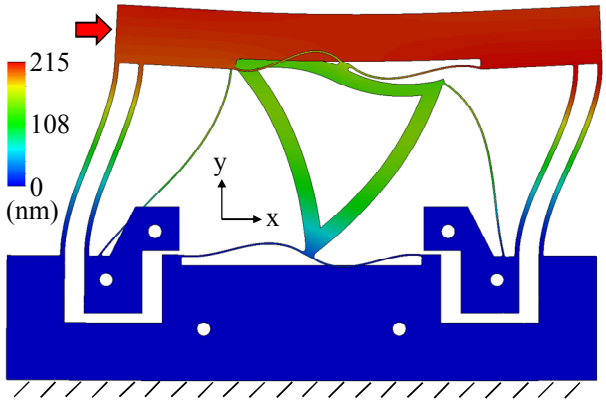

Fig. 7. FEA of the nested UE linkage design undergoing loading along the former DOF of the intermediate stage. A 1N load is applied in the x-axis on the intermediate stage (red arrow), while the final stage and grounds are held in place. The UE linkage rigid body is warped by the loading, with the top horizontal beam in the linkage forming an 'S' shape, and both of the side beams bowing in the same direction. The motion is amplified to clearly indicate the warping.

The dominant deformation was observed to be a warping of the triangular UE linkage, as shown via FEA in Fig. 7. The horizontal bar of the UE linkage deforms in an S pattern. For the remainder of the analysis, this beam will be split in half via the plane of symmetry shown in Fig. 5, and the half beam indicated with the *b1* subscript. Both the loading and the linkage are symmetric about the central plane, so the analysis needs only consider one side. The angled bars of the UE linkage, referred to via the *b2* subscript, deform via bowing. The beams' end-angle change due to loading, θ_b, at the beam intersection points, were found to be matched as is visible in Fig. 7, so θ_b can effectively be used to describe the warping of b1 and b2 that occurs as springs in parallel.

The type 1 and 2 axial forces can be related by a force and moment balance on the UE linkage, as shown in Eq. (8). Only the axial forces are considered, as with the previous analyses. The moment balance is carried out around the center of stiffness of the type 12 flexure set. The directions for each of the forces are adjusted to produce positive magnitudes as only the relative scale of the values is of interest. The resulting simple ratios of forces are also shown in Eq. (8), all linked back to F_{2a}.

$$\begin{aligned} \textstyle\sum F_x &= 2F_{11a} - 2\sin(\theta_2)F_{2a} - 2F_{12a} = 0 \\ \textstyle\sum M_z &= -2dF_{11a} - 4d\sin(\theta_2)F_{2a} = 0 \\ F_{2a} &= (1/2)\csc(\theta_2)F_{11a} = \csc(\theta_2)F_{12a} \end{aligned} \tag{8}$$

The UE linkage distortion is calculated via the application of the type 2 axial load, F_{2a}. The type 1 flexure forces are interpreted as reaction forces on pinned joints which hold the UE linkage in place. These two pinned joints are located at the center of stiffness of the type 11 flexures, as well as at the center of stiffness of the type 12 flexures. The type 2 flexure axial load produces rotation of the beam ends, captured in the rigid body force-to-rotation stiffness, $k_{b\theta}$, shown in (9). E, I, L, and h are the Young's modulus, second moment of area, effective length, and bending direction thickness (in-plane) respectively of the horizontal rigid body beam (*b1*) and angled rigid body beam (*b2*).

$$\begin{aligned} k_{b\theta} &= \frac{F_{2a}}{\theta_b} = \left(\frac{2E_{b1}I_{b1}}{L_{b1}} + \frac{2E_{b2}I_{b2}}{L_{b2}} \right) \frac{1}{d_{2b}} \\ d_{2b} &= h_{b1}\sin(\theta_2) + h_{b2}/2 \\ L_{b1} &= \left(d + d_2 - h_{b1}\right)\tan(\theta_2) - h_{b2}\sec(\theta_2) - r_1 \\ L_{b2} &= \left(d - d_2 - h_{b1}\right)\sec(\theta_2) - h_{b2}\left[\cot(\theta_2) + \tan(\theta_2)\right] \end{aligned} \tag{9}$$

The beam rotations occur together, so while their ends are fused to one another they warp at the same angle and thus the ends store no energy in resisting the warping. The dominant mode is instead captured by treating the beams as pinned-pinned with a moment applied at their linked end. The applied load is transformed to a moment via the lever arm, d_{2b}, separating the contact point of the type 2 flexures from the intersection of the b1-b2 neutral planes. The lever arm is calculated as the normal distance from a line at angle θ_2 off the y-axis passing through the extreme corner of the UE linkage, back to the intersection of the b1-b2 neutral planes. The effective lengths of the two beams are reduced by the end sections where the beams overlap one-another. The predicted warping stiffness, 270kN/rad, provides a close (<3%) match with FEA results of 280kN/rad, indicating that the model captures the dominant physics of the warping.

The rigid body warping is captured in the rigid body relaxation stiffnesses, k_{pb}. Such warping is not a concern for DOF motions, but has a noticeable effect on DOC motions, based on the scale of flexural stiffnesses and forces. The rigid body relaxation stiffnesses are explained and defined for each flexure set below.

The neck area of the UE leading to each of the type 1 flexure sets undergoes deformation during loading. This appears as a stiffness of about 40MN/m in series with the type 11 flexure (≈10MN/m axial

stiffness). The added stiffness covers the region from the end of the type 11 flexure to the intersection of the b1 beam with the central symmetry plane. A 19MN/m stiffness is observed in series with the type 12 flexure (≈10MN/m axial stiffness). The added stiffness here covers the region from the end of the type 12 flexure to the intersection of the b2 beam with the central symmetry plane. The k_{pb} expressions combine the two dominant stiffnesses: the shear of the neck region and the UE linkage warping, as shown in Eq. (10), where G_n, A_n, and L_n are the shear modulus, cross sectional area and length, respectively, of the neck shear region. d_{11b} and d_{12b} are the lever arms that transform the rigid body warping into axial translation for the type 11 and type 12 flexures, respectively.

$$k_{11b} = \frac{G_n A_n}{2L_n} + \frac{k_{b\theta}}{d_{11b}} 2\sin(\theta_2)$$
$$k_{12b} = \frac{G_n A_n}{2L_n} + \frac{k_{b\theta}}{d_{12b}} \sin(\theta_2) \qquad (10)$$

The first term accounts for the shear in the neck region, which is similar for both flexure sets. This region is typically fairly short, as it need only allow for the machining kerf width and UE rotation. The shear stiffness term is divided by 2 as the loads paths from both flexures in the set overlap in the neck, resulting in half the stiffness found by only considering one of the flexures in the set. The second term is the warping stiffness from F_{2a} to θ_b of the UE linkage body as described in Eq. (9) transformed from a rotational output to a translation along the flexure axis by a lever arm. This arm can be related to existing geometry for the type 11 flexure set, where $d_{11b} \approx d_2$, however the lever arm for the type 12 flexure set has more design freedom and can be set to a wide range of values, including ≈0. F_{2a} is replaced by an equivalent axial load function of F_{11a} or F_{12a}, via Eq. (8).

Equation (10) predicts rigid body relaxation stiffnesses of 41 MN/m for the type 11 flexures and 18 MN/m for the type 12 flexures, both of which are within 5% of FEA values, suggesting the model captures the dominant physics. The warping stiffness is the dominant term and is approximately 10x lower than the shear stiffness. This indicates that further improvement is mainly to be found in improving the warping mode. A topological alteration like the placement of an 'X' cross brace in the center gap of the UE linkage would connect the centers of the b1 and b2 beams from opposite sides, centers which move in opposite directions during the warping.

The arms of the UE linkage undergo deformation along the axis of the type 2 flexures during loading. This appears as a stiffness of about 20MN/m in series with the type 2 flexure (≈6MN/m axial stiffness). The added stiffness covers the region from the end of the type 2 flexure to the two pinned joints described for Eq. (9), which are considered the grounding points. The expression for k_{2b} combines three stiffnesses: end shear, truss stretching, and the UE linkage warping, as shown in Eq. (12). The end shear stiffness, k_{b3t}, is calculated as shown in Eq. (11), where F is a transverse load applied to the small end of a beam with shear modulus G_{b3}, whose length is L_{b3}. The beam cross section, $A_{b3}(x)$, is the product of a constant width, b_{b3}, and a varying thickness which is a maximum at the base and decreases with distance, x, along the beam at slope $\cot(\theta_2)$ until reaching a minimum of h_{b30} at the free end of the beam.

$$\frac{F}{k_{b3t}} = \int \frac{F}{G_{b3} A_{b3}(x)} dx \quad where \quad A_{b3}(x) = b_{b3}\left[h_{b30} + \cot(\theta_2)\left(L_{b3} - x\right)\right]$$
$$k_{b3t} = \frac{G_{b3} b_{b3} \cot(\theta_2)}{\ln\left[1 + \cot(\theta_2)\left(L_{b3}/h_{b30}\right)\right]} \tag{11}$$

The end shear stiffness term mimics the shear of the triangular section where the type 2 flexure anchors to the UE linkage. Shear was confirmed to be the dominant loading in this region via FEA. The stiffness was found by integrating the transverse shear over a linearly increasing cross section, which extended about 13mm, at which point beams b1 and b2 separate from one another and end the triangular segment. The type 2 axial load is applied at angle θ_2 off of transverse, which is accounted for by the secant term in Eq. (12).

$$k_{2b} = k_{b3t} \sec(\theta_2)^2 \left[k_{b1a} \sin(\theta_2)^2 + k_{b2a} \cos(2\theta_2)^2\right] k_{b\theta} d_{2b}^{-1}$$
$$k_{b1a} = \frac{E_{b1} A_{b1}}{\left(d + d_2\right)\tan(\theta_2)} \qquad k_{b2a} = \frac{E_{b2} A_{b2}}{\left(d - d_2\right)\sec(\theta_2)} \tag{12}$$

The second term in k_{2b} is the truss stiffness. This is derived from a model of the UE linkage where the b1 and b2 beams are treated as trusses with pinned ends at the joint locations described for Eq. (9). The axial stiffnesses, k_{b1a} and k_{b2a} for the b1 and b2 beams respectively, far exceed each beam's transverse and moment stiffness, so the truss model is effective. The third term in k_{2b} is the UE linkage warping stiffness. The warping angle, θ_b, of the rigid body is transformed back to an axial translation via the previously defined lever arm d_{2b}.

The net value of k_{2b} is predicted to be about 19MN/m, within 5% of FEA values, suggesting the model captures the dominant physics. The warping stiffness and the truss stiffness are nearly equivalent, suggesting that both modes would need to be improved in order to make significant improvements. While the 'X' bracing might reduce the warping mode, this would provide little benefit for the truss mode.

The ratio of the k_{pb}-and-flexure combined axial stiffness divided by the flexure-only axial stiffness can be considered the 'DOC stiffness efficiency' figure-of-merit for the rigid body deformation. This ratio approaches unity via improvements in UE linkage design. Both flexure types 1 and 2 operate with DOC stiffness efficiencies of about 75%. Further rigidification of the UE linkage may raise this value, however relatively minor gain is to be had given the tradeoff of increasing mass. The introduction of the UE linkage raises k_i by 44dB (168x) from 40kN/m to 6.7MN/m, while the DOC stiffness efficiency draws this back down by about 2.4dB (0.75x) from 6.7MN/m to 5.1MN/m. Best design principles thus suggest that there is little point in adding mass to the UE linkage in an attempt to raise DOC stiffness efficiency when significantly greater returns may be found by simply directly raising the flexure's DOC stiffness. This could be done by increasing the axial stiffness of the type 1 and/or type 2 flexures. The type 2 flexures compose the lowest stiffness component in the present design. Increasing their axial stiffness would result in the largest proportional gains in intermediate stage stiffness when the sensitivity of Eq. (6) is considered with respect to each of the flexure types.

6. Experimental Setup

Meso-scale (30cm x 30cm) DP flexures with and without the nested UE linkage were monolithically fabricated from 1.27cm thick aluminum using abrasive waterjet cutting. The nested UE linkage was intended to boost the natural frequency of the translational DOF of the intermediate stage by around 10x with only minimal (<10%) alterations to the main DOF static and dynamic performance.

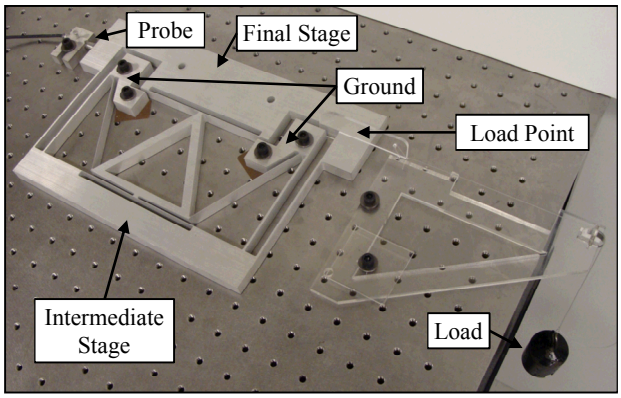

Fig. 8. Flexure DP with nested linkage, attached to optical table. This general setup was used to capture the static and dynamic properties of the main DOF as well as the underconstrained DOF.

The flexure bearings were anchored to an optical table as shown in Fig. 8, and the static/dynamic performance of both the final and intermediate stage translational DOFs were measured. Static tests were performed with weights for loading and Lion Precision capacitance probes for sensing. Dynamic tests were performed with impulse loading using a small metal tapping probe and the same sensors sampling at 50khz. The Fourier transform of the impulse response was used to determine the frequency response of the bearing, assuming the bandwidth of the impulse was well above the bandwidth of interest. This assumption is validated by the measurements shown in Fig. 9. A second order decaying sinusoid was fit to the capacitance probe readings of the impulse response in order to determine the resonance frequency. The final stage was anchored during the intermediate stage measurements.

7. Results

7.1. Small Displacement

The static and dynamic performance of both the main translational DOF and the intermediate stage translational DOF are shown in Table 2. This was done in order to demonstrate the capability of the nested linkage UE to remove the underconstrained DOF in double parallel flexure bearings. The DP flexure bearing as shown in Fig. 2 is compared to a DP bearing with the nested UE linkage as shown in Fig. 5. Measurements are compared against FEA predictions and theoretical predictions from the equations described previously. The base was grounded and an x-axis force was applied to the side surface of the final stage for the final stage DOF analysis. The base and the final stage were grounded and an x-axis force was applied to the side of the

intermediate stage for the intermediate stage DOF analysis, as shown in Fig. 7. Displacement was measured from the center of the stage.

Table 2. Static and Dynamic Performance of Bearing DOFs

	DP			DP with nested UE			
	Measured	**FEA**	**Theory**	**Measured**	**FEA**	**Theory**	**Units**
Final Stage DOF							
k_f	9.76±0.25	9.71	9.98	10.9±1.2	10.5	10.7	kN/m
ω_{nf}	19.1±0.1	20.3	20.6	20.7±0.1	20.9	21.0	Hz
Intermed. Stage DOF							
k_i	38.3±0.3	38.8	39.9	5130±190	4890	5070	kN/m
ω_{ni}	60.4±0.3	67.9	65.8	650±3	648	732	Hz
Stiffness Ratio							
k_i/k_f	3.92±0.11	4.00	4.00	471±55	466	474	--

Evidence of underconstraint removal is found in the static analysis via the UE-driven increase in the stiffness ratio k_i/k_f. Relative stiffness can be used to identify DOF [6,10]. Table 2 indicates that the intermediate stage DOF has been moved from a DOF-scale stiffness ratio of ≈4 to a DOC scale stiffness ratio of about 470 [10]. The underconstrained DOF has been effectively removed from the system, and the nested linkage has thus performed as intended. The main translational DOF shows minimal changes in both static (12%) and dynamic (8%) performance due to the addition of the nested linkage. The dynamic change is partially cancelled as both the stiffness and inertia rise. The intermediate stage DOF shows significant changes in both static (134x) and dynamic (11x) performance, also as desired. The measurements confirm that the accuracy of both the FEA (max 4.7%, average -2%, standard deviation 2.4%) and the analytical model (max 4.2%, average 0.86%, standard deviation 2.5%) are sufficient for use as flexural geometry design tools.

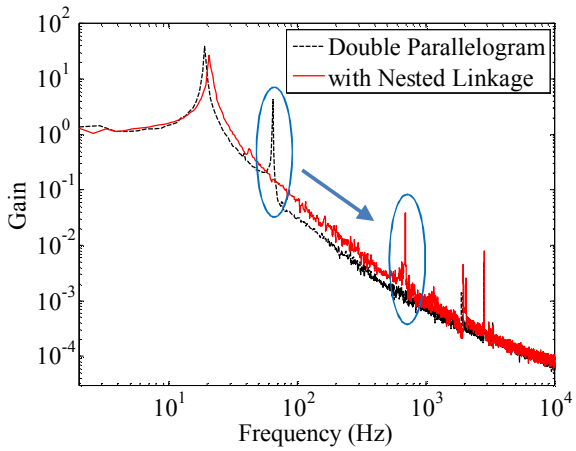

Fig. 9. The Bode gain plot for the unaugmented DP flexure is compared to that of the DP flexure with the nested linkage. The intermediate stage resonance has been shifted from 60hz to 650hz, while the main stage resonance has been changed by only ≈5%.

The net effect of the nested UE is clearly seen in Fig. 9, where the Bode gain plots for the flexures with and without the UE are shown. These response plots were generated via the Fourier transform of the impulse response data. The low frequency gain for both setups was normalized to unity in order to make the charts directly comparable. The intermediate stage would normally generate a problematic resonance only slightly above the main translational DOF resonance; however this has been shifted over 10x higher without significant impact to the dynamics of the main DOF.

7.2. Large Displacement

A second effect of underconstraint on DP bearings, as described in the introduction, is a reduction in large displacement y-axis stiffness. This effect was analyzed via FEA as a redundant confirmation of the capabilities of the nested UE design to remove underconstraint.

FEA analysis of the DP and DP with UE bearings were carried out for both force and displacement control on the final stage. Theory and literature suggest there should be no difference between these two control methods. The bearing stiffness is commonly parameterized to a controlled displacement [1,25], however controlled force can be a more accurate model in certain conditions. The high-bandwidth pullin effects on comb drives will likely occur before the main DOF controller has time to react and hold to a certain displacement, assuming closed loop control. Both constraints were used in the FEA for comparative purposes, as shown in Fig. 10. The displacement of the final stage, δ, was normalized by the thickness of the

type-m flexures h_m, and represented by $X=\delta/h_m$. The FEA was carried out to $X\approx$20-30, as the simulations had difficulty in converging past this scale.

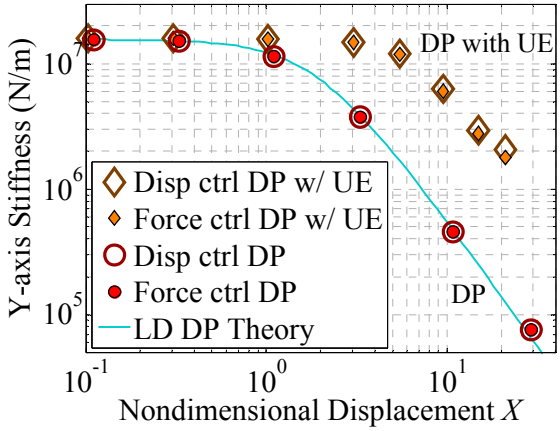

Fig. 10. Logarithmic plot of axial stiffness vs nondimensional displacement, showing large displacement effects. Both simple DP and DP with UE stage displacements were simulated using large displacement FEA with displacement (hollow points) and force (solid points) control on the final stage. The DP results are compared to models presented in literature (LD DP Theory) [25]**.**

The controlled force FEA results are shown as the solid marks, while the controlled displacement FEA results are shown as the hollow marks, in order to enable easy comparison of the values. The force and displacement control diverge slightly at the large displacement, likely due to stage warping. The DP bearing results are compared to the literature (LD DP) analysis. The DP with UE shows a significantly higher dropoff scale (≈15 vs ≈1.7), clearly indicating the removal of the underconstraint in the DP bearing.

8. Conclusions

We have demonstrated an improved flexure linkage design for selectively removing the underconstraint in a DP linear flexural bearing. Detailed models are provided for the small displacement behaviors as well as dynamics. The new design reduces many of the problems associated with existing solutions, such as static/dynamic performance degradation, increased footprint, and design coupling, all of which limit the applicability of underconstraint elimination designs in flexural bearings. The new nested UE linkage design will enable wider use of the UE concept as well as improving device performance where replacing existing UE designs.

The modified linkage is shown to work within 5% error of the small displacement predictions generated by analytical models described in this paper. The models and LDES figure-of-merit provides a new tool for designing large displacement bearings, and can be applied to other UE designs. The linkage is successful at selectively boosting the stiffness (134x) and resonance (11x) of the translational DOF of the intermediate stage without significantly impacting (<12%) the main translational DOF of the final stage. This design topology is readily implemented in existing structures owing to its compact structure and well modeled performance.

9. Acknowledgments

Part of the research for this publication was conducted while at the Massachusetts Institute of Technology. This work was funded by the Institutional Postdoc Account (31006/12.1.1.A.4), and performed under the auspices of the U.S. Department of Energy by Lawrence Livermore National Laboratory under Contract DE-AC52-07NA27344. LLNL-JRNL-656683.

10. References

[1] Awtar S, Slocum AH, Sevincer E. Characteristics of Beam-Based Flexure Modules. J Mech Des 2007;129:625–39.

[2] Brouwer DM, Otten A, Engelen JBC, Krijnen B, Soemers HMJR. Long-range Elastic Guidance Mechanisms for Electrostatic Comb-drive Actuators. Proc. EUSPEN Int. Conf., 2010.

[3] Saggere L, Kota S, Crary SB. A New Design for Suspension of Linear Microactuators. Proc. 1994 Int. Mech. Eng. Congr. Expo. Dyn. Syst. Control, Chicago: 1994, p. 671–6.

[4] Slocum A. Precision Machine Design. Eaglewood Cliffs, NJ: Prentice-Hall, Inc.; 1992.

[5] Blanding DL. Exact constraint: machine design using kinematic principles. ASME Press; 1999.

[6] Smith ST. Flexures: Elements of Elastic Mechanisms. CRC Press; 2000.

[7] Hopkins JB, Culpepper ML. Synthesis of multi-degree of freedom, parallel flexure system concepts via Freedom and Constraint Topology (FACT) – Part I: Principles. Precis Eng 2010;34:259–70.

[8] Hopkins JB, Culpepper ML. Synthesis of multi-degree of freedom, parallel flexure system concepts via freedom and constraint topology (FACT). Part II: Practice. Precis Eng 2010;34:271–8.

[9] Panas RM, Cullinan MA, Culpepper ML. Design of piezoresistive-based MEMS sensor systems for precision microsystems. Precis Eng 2012;36:44–54.

[10] Awtar S. Synthesis and Analysis of Parallel Kinematic XY Flexure Mechanisms. Massachusetts Institute of Technology, 2004.

[11] Brouwer DM, de Jong BR, Soemers HMJR. Design and modeling of a six DOFs MEMS-based precision manipulator. Precis Eng 2010;34:307–19.

[12] Xu Q, Li Y. Novel Design of a Totally Decoupled Flexure-Based XYZ Parallel Micropositioning Stage. 2010 IEEE/ASME Int. Conf. Adv. Intell. Mechatronics, Montreal, Canada: IEEE; 2010, p. 866–71.

[13] Seggelen JK v., Rosielle PCJN, Schellekens PHJ, Spaan HAM, Bergmans RH, Kotte GJWL. An Elastically Guided Machine Axis with Nanometer Repeatability. CIRP Ann - Manuf Technol 2005;54:487–90.

[14] Yangmin Li, Qingsong Xu. Design and Analysis of a Totally Decoupled Flexure-Based XY Parallel Micromanipulator. IEEE Trans Robot 2009;25:645–57.

[15] Parmar G, Barton K, Awtar S. Large dynamic range nanopositioning using iterative learning control. Precis Eng 2014;38:48–56.

[16] Hao G, Kong X, Meng Q. Design and Modelling of Spatial Compliant Parallel Mechanisms For Large Range of Translation. Proc. ASME 2010 Int. Des. Eng. Tech. Conf. Comput. Inf. Eng. Conf. IDETC/CIE 2010, vol. 44, Quebec, Canada: 2010.

[17] Slocum AH. Precision Machine Design. Dearborn, MI: SME; 1992.

[18] Pusl KE. Folded Spring Flexure Suspension For Linearly Actuated Devices. US7550880B1, 2009.

[19] Van Eijk J. On the design of plate-spring mechanisms. Delft University of Technology, 1985.

[20] Zhou G, Dowd P. Tilted folded-beam suspension for extending the stable travel range of comb-drive actuators. J Micromechanics Microengineering 2003;13:178–83.

[21] Brouwer DM, Jong BR De, Soemers HMJR, Dijk J Van. Sub-nanometer stable precision MEMS clamping mechanism maintaining clamp force unpowered for TEM application. J Micromechanics Microengineering 2006;16:S7–S12.

[22] Chang S, Wang CS, Xiong CY, Fang J. Nanoscale in-plane displacement evaluation by AFM scanning and digital image correlation processing. Nanotechnology 2005;16:344–9.

[23] Krijnen B, Brouwer DM. Position control of a MEMS stage with integrated sensor. Proc. 11th EUSPEN Int. Conf., Como, Italy: 2011, p. 2–3.

[24] Olfatnia M, Sood S, Awtar S. Note: an asymmetric flexure mechanism for comb-drive actuators. Rev Sci Instrum 2012;83:116105.

[25] Olfatnia M, Sood S, Gorman JJ, Awtar S. Large Stroke Electrostatic Comb-Drive Actuators Enabled by a Novel Flexure Mechanism. J Microelectromechanical Syst 2013;22:483–94.

[26] Trutna TT, Awtar S. An Enhanced Stability Model for Electrostatic Comb-Drive Actuator Design. Proc. ASME 2010 Int. Des. Eng. Tech. Conf. Comput. Inf. Eng. Conf. IDETC/CIE 2010, Montreal, Canada: 2010, p. 1–9.

[27] Ferreira PM, Dong J, Mukhopadhyay D. High Precision Silicon-On-Insulator MEMS Parallel Kinematic Stages. US8310128B2, 2012.

[28] Jaecklin VP, Linder C, Rooij NF De, Moret JM, Bischof R, Rudolf F. NOVEL POLYSILICON COMB ACTUATORS FOR XY-STAGES. Proc. IEEE Micro Electro Mech. Syst. '92, Travemunde: 1992, p. 147–9.

[29] Jones R V, Phil D, Young IR. Some parasitic deflexions in parallel spring movements. J Sci Instrum 1956;33:11–5.

[30] Jones R V. Some uses of elasticity in instrument design. J Sci Instrum 1962;39:193–203.

[31] Brouwer D. Design Principles for Six Degrees-of-Freedom MEMS- based Precision Manipulators. University of Twente, 2007.

[32] Hopkins JB, Culpepper ML. Synthesis of precision serial flexure systems using freedom and constraint topologies (FACT). Precis Eng 2011;35:638–49.

[33] Franklin GF, Powell JD, Naeini AE. Feedback Control Of Dynamic Systems - 5th edition. 5th ed. Upper Saddle River, NJ: Prentice Hall,2005; 2006.

[34] Plainevaux JE. Guidage rectiligne sur lames élastiques. Comparaison de divers types connus et nouveaux. Nuovo Cim 1954;12:37–59.

[35] Plainevaux JE. Mouvement parasite vertical d'une suspension élastique symétrique à compensation et asservissement. Nuovo Cim 1954;11:626–38.

[36] Smith ST. Mechanical Systems in Nanometre Metrology. University of Warwick, 1987.

[37] Valois M. Linear Flexure Bearing. US 2013/0015616 A1, 2013.

[38] Genequand P-M. Device for the Guidance in Rectilinear Translation of an Object that is Mobile in Relation to a Fixed Object. US 6059481, 2000.

[39] Suh NP. Axiomatic Design: Advances and Applications. Oxford University Press; 2001.

[40] Smith ST. Foundations of Ultra-Precision Mechanism Design. CRC Press; 2003.

[41] Jerman JH, Grade JD. Miniature device with translatable member. US 6664707 B2, 2003.